

# Frequency to power conversion by an electron turnstile

Marco Marín Suárez (✉ [marco.marinsuarez@aalto.fi](mailto:marco.marinsuarez@aalto.fi))

Aalto University <https://orcid.org/0000-0003-2057-7707>

Joonas Peltonen

Aalto University School of Science <https://orcid.org/0000-0002-3903-7623>

Dmitry Golubev

Aalto University <https://orcid.org/0000-0002-0609-8921>

Jukka Pekola

Aalto University School of Science

---

## Research Article

**Keywords:** frequency to power conversion, single-electron transistor, electron turnstile

**Posted Date:** August 4th, 2021

**DOI:** <https://doi.org/10.21203/rs.3.rs-745026/v1>

**License:** © ⓘ This work is licensed under a Creative Commons Attribution 4.0 International License.

[Read Full License](#)

---

**Version of Record:** A version of this preprint was published at Nature Nanotechnology on January 20th, 2022. See the published version at <https://doi.org/10.1038/s41565-021-01053-5>.

# Frequency to power conversion by an electron turnstile

Marco Marín-Suárez,<sup>1,\*</sup> Joonas T. Peltonen,<sup>1</sup> Dmitry S. Golubev,<sup>1</sup> and Jukka P. Pekola<sup>1,2</sup>

<sup>1</sup>*Pico group, QTF Centre of Excellence, Department of Applied Physics, Aalto University, FI-000 76 Aalto, Finland*

<sup>2</sup>*Moscow Institute of Physics and Technology, 141700 Dolgoprudny, Russia*

**Direct frequency to power conversion (FPC), to be presented here, links both quantities through a known energy, like single-electron transport relates an operation frequency  $f$  to the emitted current  $I$  through the electron charge  $e$  as  $I = ef$  [1–6]. FPC is a natural candidate for a power standard resorting to the most basic definition of the watt, comprising a simple and elegant way to realize it [7]. In this spirit, single-photon emission and detection at known rates have been proposed and experimented as radiometric standard [8–15]. However, nowadays power standards are only traceable to electrical units with no alternative proposals in sight [7, 16–18]. In this letter, we demonstrate the feasibility of solid-state direct FPC using a SINIS (S = superconductor, N = normal metal, I = insulator) single-electron transistor (SET) accurately injecting  $N$  (integer) quasiparticles (qps) per cycle to both leads with discrete energies close to their superconducting gap  $\Delta$ , even at zero drain-source voltage. Furthermore, the bias voltage plays an important role in the distribution of the power among the two leads, allowing for an almost equal injection  $N\Delta f$  to the two. We estimate that under appropriate conditions errors can be well below 1%.**

The FPC relation can be understood based on a simplified picture of a driven NIS junction (Fig. 1a) by looking at the qp injection dynamics. The key property here is the singularity of the superconducting density of states at energies  $\pm\Delta$  as counted from the Fermi level. During the driving period where the chemical potential of N is periodically shifted, an electron tunnels into the superconductor with energy  $\sim \Delta$  due to this diverging density of states. Later on, the driving provides enough energy for an electron to tunnel into the island breaking a Cooper pair and leaving an excitation in the superconductor, again close to the gap-edge. Thus, two tunnelling events per cycle occur; for larger driving amplitudes a higher even number  $2N$  of tunnelling events is allowed. Within this picture, if a second superconducting lead is tunnel coupled to the island, the tunnelling events at bias voltage  $V_b = 0$  occur stochastically through either junction with probabilities proportional to each junction transparency. This whole operation results in total energy injection of nearly  $2N\Delta$  in each cycle in the absence of net current. The case for a biased ( $V_b \neq 0$ ) SINIS

SET is depicted in Figure 1b in which the qp injection events happen analogously to panel b. The only difference is that the bias defines a preferred direction for the charge transfer and therefore there will be  $N$  tunnelling events per junction, i.e., the junction transparency does not play a key role anymore. The total energy injected is distributed almost equally to both leads but remains (nearly) unchanged. Time-averaged, the total injected energy current would be given by

$$P = 2N\Delta f, \quad (1)$$

and would exhibit a structure of plateaus similar to the charge current pumped through SINIS turnstiles [3], but now even at zero bias voltage. Accuracy of Eq. (1) can be tested in the FPC device depicted in Fig. 1c (see Supplementary Section S1 for its characterization).

This device constitutes a turnstile for single electrons (see Supplementary Figure S1) when the island (light red short structure in Figure 1c) is periodically driven at frequency  $f$  with a radio-frequency (rf) signal applied to a capacitively coupled gate electrode. At proper source-drain biases and driving amplitudes, an average charge current  $I = Nef$  is obtained. This current is transported by  $Nf$  qps injected per second to both tunnel-contacted leads (light blue short structure in Fig. 1c), respectively. The qps transport energy approximately without losses across the narrow leads [19, 20] to directly interfaced normal-metal traps (light red long structures). These structures act as bolometers for measuring quantitatively the heat generated by the qp injection, accounting completely for the power [21]. This heat can be determined within the conventional normal-metal electron-phonon interaction model [22] as  $P = \Sigma V (T_e^5 - T_b^5)$ . Here  $\Sigma$  is the electron-phonon coupling constant of the material,  $V$  the trap volume,  $T_e$  its electron temperature and  $T_b$  the phonon bath temperature which usually can be taken as the cryostat temperature [23]. The bolometer is calibrated *in-situ*. See Supplementary Section S2 for details on the calibration of this detector.  $T_e$  is in turn obtained by current-biasing the superconducting tunnel probes (vertical blue structures in Fig. 1c) contacted to the trap and measuring the corresponding voltage drop (see Supplementary Section S3 for the temperature calibration of these thermometers). The measured power can be compared to the expected FPC outcome.

The main result of this work is shown in Fig. 2 where the total injected power  $P_T$  (to the left  $P_L$  plus to the right lead  $P_R$ ) measured with the bolometers is shown. This was measured with a gate signal  $V_g =$

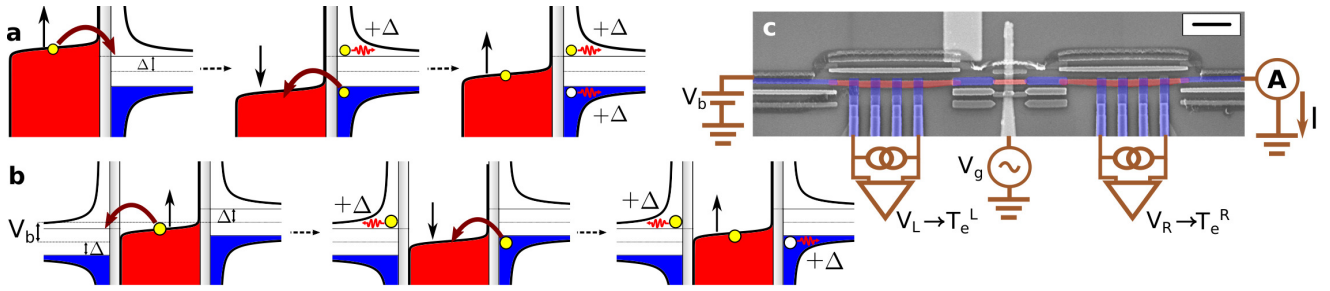


FIG. 1. **Single-electron turnstile for FPC.** (a) Sketch illustrating the operation at zero bias exemplified in a hybrid single-electron box. The chemical potential of the N electrode (left) is varied periodically. First, an electron (yellow dot) has enough energy to be injected into the S lead (right) at the gap edge from the island as an excitation. Later, the driving enables an electron to tunnel from the lead to the island while the previously injected excitation diffuses. Once this electron tunnels to the island, it leaves one excited state close to the gap edge in the lead. Total energy of  $2\Delta$  is injected into the lead per cycle. In the case of a turnstile at zero bias, the operation is the same as here, but the tunnelling events occur stochastically through the two contacts. (b) Sketch illustrating the non-zero bias behaviour in FPC. As opposed to the zero bias case, the excitations are created in both leads, giving again a total injected energy of  $2\Delta$  per cycle distributed equally to the two leads. (c) Experimental setup for measuring the injected power in the turnstile operation together with a coloured scanning electron micrograph. Light red refers to normal-metal and blue to superconductor. Scale bar is  $1 \mu\text{m}$ .

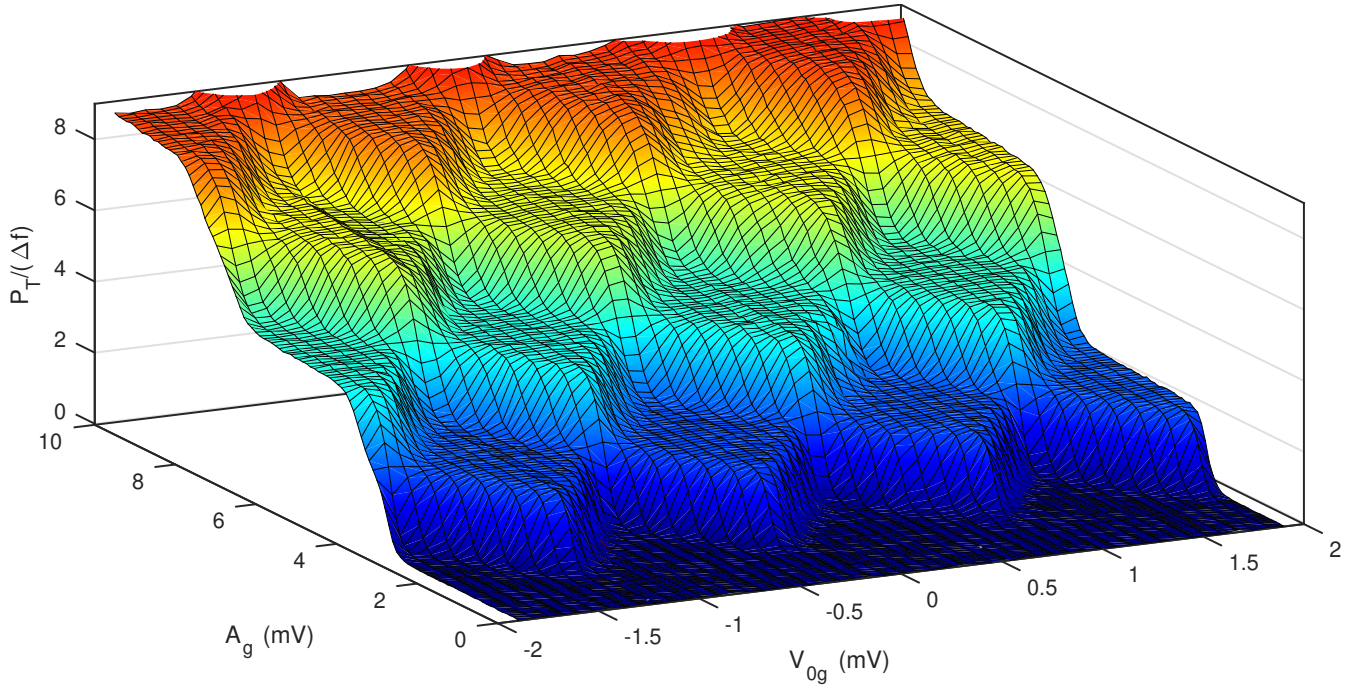


FIG. 2. **Power injection at zero bias.** Total injected power at  $f = 80 \text{ MHz}$  and  $V_b = 0$  measured at  $T_b = 130 \text{ mK}$  as a function of the gate offset  $V_{0g}$  spanning several periods. The power is ideally given by  $P = 2N\Delta f$  with  $N$  an integer. Here the gate amplitude  $A_g$  range is such that four pumping plateaus become visible. It is evident that the injected power follows the diamond pattern, here even in the absence of average current through the device.

<sup>96</sup>  $V_{0g} + A_g \sin(2\pi ft)$  at  $f = 80 \text{ MHz}$  and  $V_b = 0$ , hence<sup>104</sup>  
<sup>97</sup> no net charge (particle) current flows through the SET.<sup>105</sup>  
<sup>98</sup> Here, the DC gate voltage is swept over various gate peri-<sup>106</sup>  
<sup>99</sup> ods revealing the  $e$ -periodic nature of the injected energy.<sup>107</sup>  
<sup>100</sup> Simultaneously, the signal amplitude is varied so that the<sup>108</sup>  
<sup>101</sup> gate-induced charge spans several charge stability regions<sup>109</sup>  
<sup>102</sup> in the Coulomb diamonds of the SET. The measured in-<sup>110</sup>  
<sup>103</sup> jected power exhibits plateaus of (approximately) con-<sup>111</sup>

stant value against  $V_{0g}$  and  $A_g$ , following closely Eq. (1) confirming the dynamics described in Figs. 1a and 1b. Therefore, we can assert that excitations are being injected close to the superconductor gap edge. The similarity of the plateaux pattern with that of Figure 2a in Ref. 3 is evident and shows parallelism between the frequency to current conversion of single-electron transport and our proposal of frequency to power conversion,

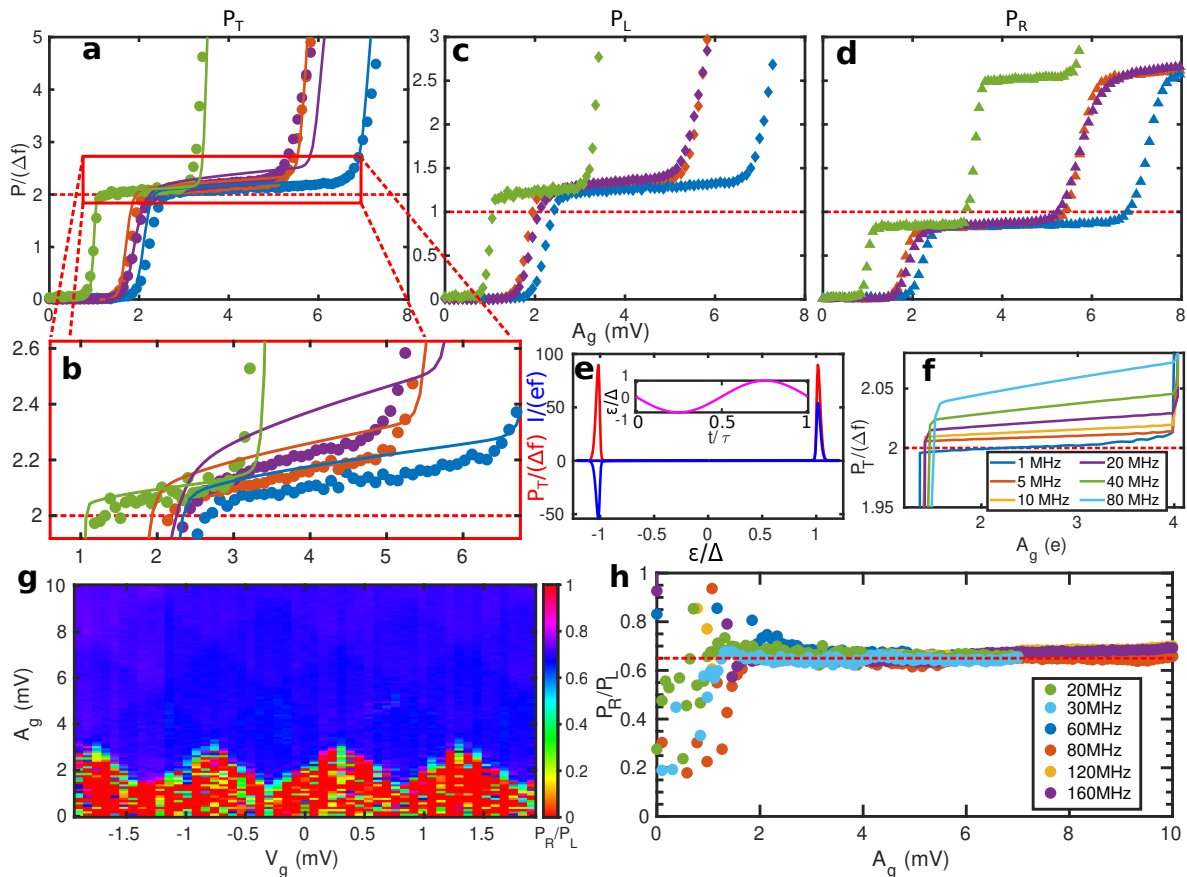


FIG. 3. **Power injection at zero bias.** (a) Power injected to the two leads in the absence of average current ( $V_b = 0$ ) and at offset equivalent to  $n_g = 0.5$ , showing that a power  $\sim 2\Delta f$  for different driving frequencies is generated in the first plateau. Solid lines are calculated and data measured at  $T_b = 117$  mK, colors correspond to the legend of panel (h). (b) Close-up of panel (a) to the first power plateau, showing how the calculated curves follow the trend of the data. (c) Power injected into the right lead and (d) into the left lead. (e) Simulation of instantaneous total injected power (red line) and current (blue line) as a function of the chemical potential difference for a jump into the island. The inset shows how this energy evolves within one sinusoidal driving cycle with a gate amplitude above the onset of the first plateau. Here, the measured device parameters are used and  $f = 5$  MHz,  $T_S^L = T_S^R = T_N = 10$  mK. (f) Total injected power plateaus calculated for a turnstile with more optimized, but realistic, parameters (see the text) and with triangular gate driving. (g) Measured ratio between the injected power in the right and left leads as a function of the gate offset and amplitude, here the data are the same as in Fig. 2. Notice that this ratio is insensitive to the varied parameters and equal to the inverse of the normal-state junction resistance ratio. (h) Ratio between the injected power in the right and left leads at several driving frequencies and gate amplitudes, data from panels (c) and (d).

112 the latter being possible at wider bias ranges including 126  
 113  $V_b = 0$ . 127

114 Further measurements of the power production at zero 128  
 115 bias are shown in Fig. 3. Panel 3a shows the total in- 129  
 116 jected power with  $V_{0g}$  at gate open position for a wide 130  
 117 range of driving frequencies and confirms the results of 131  
 118 Fig. 2 at different injected powers. The transmission of 132  
 119 the rf gate voltage depends on frequency giving different 133  
 120  $A_g$  dependences of the otherwise similar power (and cur- 134  
 121 rent) curves for different frequencies. Panel b shows that 135  
 122 the total generated energy is close to ideal FPC. Calcula- 136  
 123 tions (solid lines) of the generated power resulting from 137  
 124 a Markovian model (used also for DC characterization, 138  
 125 See Supplementary Section S4) can reproduce the gate 139

amplitude and frequency dependencies. Panels c and d  
 exhibit the individual contributions to the power in the  
 left and right lead, respectively. Notice that the two are  
 not equal as explained above.

More insight into the dynamics of the zero bias opera-  
 tion is gained by simulating the instantaneous behaviour  
 of the device. Figure 3e shows the calculated total in-  
 jected power (red curve) and the current through one  
 junction (blue curve) as function of the energy change of  
 an electron tunnelling into the island  $\varepsilon = 2E_c(0.5 - n_g)$ .  
 Here  $E_c$  is the system charging energy and  $n_g = C_g V_g/e$   
 is the normalized island excess charge induced by the  
 gate voltage. A driving signal with offset equivalent to  
 $n_g = 0.5$ , as used for most of the measurements at  $V_b = 0$ ,

and period  $\tau$  induces the evolution in  $\varepsilon$  shown in the inset of Figure 3e for a driving amplitude at the start of the first plateau. It is clear that only electrons within a narrow energy band around  $\Delta$  tunnel in and out of the island through the same junction, cancelling current and injecting an energy  $\Delta$  per event as postulated. Naturally, the tunnelling events can happen through any junction. How often a given junction is involved depends on the relative transparencies to be explained below.

Although the measured total injected powers shown in Figs. 2 and 3a are not exactly  $2\Delta$  in the first plateau we show in Fig. 3f that a system with proper  $E_c$ , total normal-state junction resistance  $R_T$  and Dynes parameter [24]  $\eta$  can inject a power closer to this value. In this panel the total injected power for a device with  $E_c = \Delta = 200 \mu\text{eV}$ ,  $R_T = 200 \text{k}\Omega$  and  $\eta = 10^{-6}$  was calculated solving the same Markovian model used so far with low but achievable temperatures ( $T_S^L = T_S^R = 150 \text{mK}$ ,  $T_N = 10 \text{mK}$ , for left and right lead and island respectively). From there it is possible to see that when the driving is slow enough ( $f = 1 \text{MHz}$ ) the accuracy of the injected power is within 0.20% and 0.65% in the first plateau and between 1.27% and 3.8% for  $f = 80 \text{MHz}$ . Therefore it is possible, in principle, to achieve a power injection of  $2\Delta$  with small deviations given that  $\eta$  is sufficiently small and temperatures are low. Under these conditions the ultimate limitation of accuracy would then be determined by the capability of measuring small powers bolometrically: at 1 MHz the power is 0.3 fW which exceeds the noise level in a standard setup by two orders of magnitude [25]. Additionally, we have verified that injection errors scale as  $(E_c e^2 R_T f / \Delta^2)^{2/3}$ , thus higher power emission with smaller inaccuracy is possible for more transparent junctions. Yet in this argument we ignore the influence of Andreev tunnelling power injection [26].

How the power is distributed to the two leads can be easily understood within the Markovian model (see details in Supplementary Section S5). The absence of a preferred direction of flow (i.e., the bias voltage) together with assuming the same qp temperature for both leads yield

$$\frac{P_R}{P_L} = \frac{R_L}{R_R}. \quad (2)$$

Where  $R_{L(R)}$  is the normal-state left (right) junction resistance. For the present device, we determined by the DC characterization  $R_L/R_R = 0.65$ . The ratios shown in Figs. 3g (calculated from data of Fig. 2) and 3h (from data in Figs. 3c and 3d) match this value, validating Eq. (2). Thus, the power is distributed according to the ratio of junction transparencies. Notice the insensitivity of this quantity to gate parameters or temperature.

Next, we turn to the case  $V_b \neq 0$ . Figure 4 shows two paradigmatic cases in panels a and b (see Supplementary

Section S6 for additional data). In the former, the driving is slow enough to enable fully synchronized tunnelling in the direction of bias, avoiding back-tunnelling (i.e., tunnelling against the bias). In the latter, the driving frequency is fast such that forward tunnelling is compromised and back-tunnelling may take place instead. As a result, the pumped current drops toward the end of the plateau.

In Fig. 4a driving at  $f = 20 \text{MHz}$  and  $V_b = 240 \mu\text{V}$  was applied, avoiding the back-tunnelling. An accurate single-electron current (purple dots) is emitted whose behaviour is well described by our simulations (solid black line, see inset). Similarly to the zero bias case, Eq. (1) is closely followed (see green and cyan dots for left and right leads, respectively), however now the main difference lies in how the injected energy is distributed between the leads. The bias, and consequently a preferred direction of tunnelling enable an almost equal share in the power injection to both leads, following the dynamics described in Fig. 1b. Both experiment and simulations show that now the distribution of the power has been inverted with respect to the zero bias case, i.e.  $P_R \gtrsim P_L$ . This can be explained by arguing that more energy needs to be provided for tunnelling through the more resistive junction, which is bound to happen under the present conditions before a back-tunnelling event can occur through the more transparent junction. In terms of Fig. 3e the power peaks move to  $|\varepsilon| \gtrsim \Delta$ .

On the other hand, data in Fig. 4b were measured with  $f = 60 \text{MHz}$  and  $V_b = 160 \mu\text{V}$ . Towards high gate amplitudes a small current opposed to the bias flows; this behaviour is also well caught by our simulations. The ratio  $P_R/P_L$  inverts with respect to the zero bias case for gate amplitudes close to the current onset (see the inset); this behaviour is as in panel a. When higher gate amplitudes provide enough energy to activate tunnelling opposed to the biased direction, this ratio inverts again and now the situation is analogous to the zero bias case although a preferred direction with non-vanishing net current is present in this regime. The dynamics of Fig. 1b do not hold anymore and two tunnelling events can occur through the same junction within one cycle. Naturally, this process is bound to happen more likely through the more transparent junction, therefore  $P_L$  exceeds  $P_R$  as is clear from the figure. It is also evident that, as the current approaches zero due to back-tunnelling processes the power ratio decreases. Still,  $P_R/P_L \geq R_L/R_R$ , as shown in  $P_R/P_L$  from Figure 4c, where ratios for powers measured at different frequencies at the plateau are presented as function of the applied bias. The ratio collapses to a single value for all frequencies at  $V_b = 0$ , as expected. Cartoons in Fig. 4c exemplify the processes in the two presented regimes: when the voltage bias tends to zero the two tunnelling events are uncorrelated as to in which junction they occur. Conversely, at high biases these tunnelling events occur unidirectionally, one per

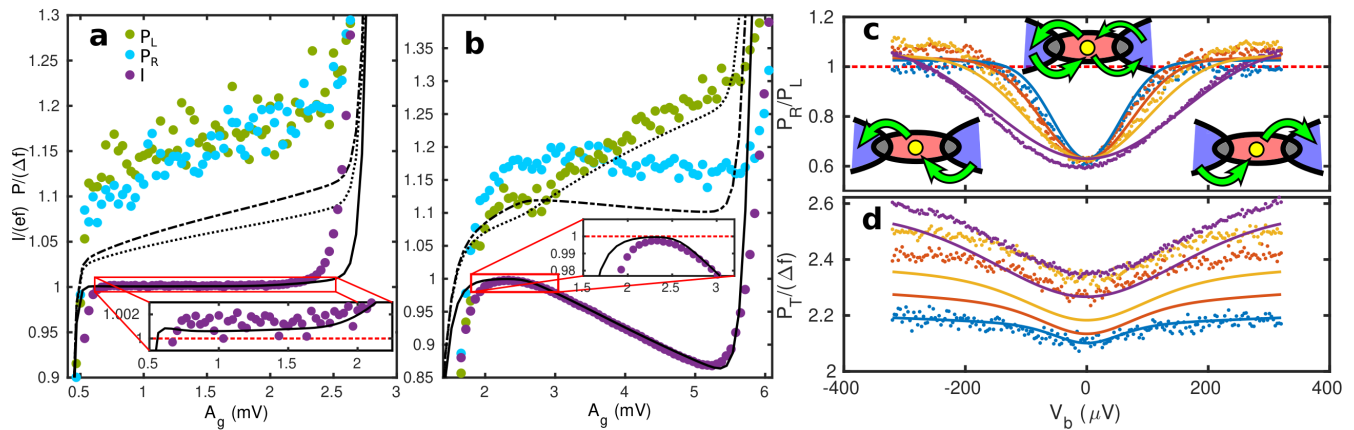


**FIG. 4. Power injection at non-zero bias.** Data measured at  $T_b = 117$  mK (a) Charge current (purple filled circles) and injected power to the left (green circles) and right (cyan circles) traps at  $V_b = 240 \mu\text{V}$  and  $f = 20$  MHz against the gate amplitude. Black lines are simulations of charge current (solid), power injected into the left (dotted) and right (dash-dotted) leads, from the Markovian model. In this situation, the power is almost equally distributed to both leads. (b) As in (a) but for  $V_b = 160 \mu\text{V}$  and  $f = 60$  MHz, here the driving rate is comparable to the tunnelling rates. As a consequence the current and power injected to the right lead plateaus bend down and therefore the less transparent junction transmits less power. (c) Measured (dots) and calculated (solid lines) injected power ratios on the first plateau for driving frequencies  $f = 30, 60, 80, 160$  MHz in blue, red, yellow and purple, respectively, as function of the bias. Two observations can be made, the ratio approaches 1 (i.e., one tunnelling event occurs per junction unidirectionally, see the cartoons) as the absolute value of bias increases (i.e., tunnelling rates increase) and it converges to  $R_L/R_R$  at  $V_b = 0$  for all the frequencies. (d) As in (c) but for the total heat injected. The heat deviates from the value  $P = 2\Delta f$  when the driving frequency becomes comparable to the tunnelling rates.

248 junction. This is also shown in Supplementary Figure S7.  
 249 For  $f = 30$  MHz (blue dots), i.e., a driving slow enough to  
 250 avoid back-tunnelling, relatively low biases give already  
 251  $P_R/P_L \approx 1$ , as expected. For higher frequencies, higher  
 252 biases are needed to drive the ratio closer to 1 (compare  
 253 Supplementary Figs. S4–S6) since  $\varepsilon$  changes at a rate  
 254 comparable to the tunnelling rates at low biases giving  
 255 rise to back-tunnelling. This fast change of  $\varepsilon$  compared  
 256 to the tunnelling rates enables electrons with a wider dis-  
 257 tribution of energies to tunnel, resulting in broader peaks  
 258 than those shown in Figure 3e, see Supplementary Figure  
 259 S8. This gives as a result the pattern of Figure 4d: for  
 260 higher frequencies excitations with energies progressively  
 261 higher than  $\Delta$  are injected into the leads. In general,  
 262 lower frequencies will give a more bias insensitive power  
 263 injection. This behaviour is accurately captured by a  
 264 Markovian model as seen from the solid lines in Figs. 4c  
 265 and 4d.

266 As to further realizations and applications, FPC could  
 267 also be realized by replacing the superconducting leads  
 268 with quantum dots having a  $\delta$ -like singular density of  
 269 states around tunable energy levels [27]. This tunability  
 270 gives the possibility to modify at will the injected en-  
 271 ergy and might allow for increasing the conversion yield.  
 272 Furthermore, the narrow highly peaked density of states  
 273 around the energy level enhances the selectivity of the  
 274 tunnelling events increasing the accuracy of the injected  
 275 power. Importantly, the precision of the injection rate is  
 276 ensured by the dot detuning from the Fermi level and the

island finite charging energy. In addition to the present demonstration, FPC might find applications in nanoscale thermodynamics as a heat pump with no net particle flow [28–31] as well as enabling a careful study of the dynamics of superconducting excitations because of the high injection control in our realization, unlike in recent injection demonstrations [32].

In summary, we have shown that a periodically driven NIS junction can be used as a synchronized power injector even in the absence of current. This is due to the singularity of the density of states in the superconducting lead which enables a high electron energy selectivity. This energy is then measured by a normal metal bolometer trapping the excitations. This, added to the possibility of injecting qps at a precisely known rate determined by the driving frequency, allows us to assert that a total power of  $2N\Delta f$  is generated. The highly controlled injection allows one to measure a power as a known energy ( $2N\Delta$ ) released at a given repetition rate ( $f$ ) providing a natural realization of the unit of power. This rationale is completely in line with the *ampere mise en pratique* based on single-electron transport [7]. Our implementation has the advantage of being a real “on-demand” precise energy source, unlike single-photon sources where emission efficiencies go up to 50% [15]. The superconducting gap can be accurately measured by standard tunnel spectroscopy or by determining the critical temperature. Further steps of optimization, for instance in driving waveforms, are needed to achieve higher accu-

racy in power transfer. Although lower injection rates allow for more accurate conversion the detection method sets a low bound for the power generation. Most importantly, suitable device parameters and environmental conditions set lower errors in power emission. Furthermore, we demonstrated that the injection of qps follows a stochastic Markovian model favouring injection through the more transparent junction when the device is unbiased. When properly biased, the same amount of power is distributed evenly to the two leads.

## METHODS

### Fabrication

The samples were fabricated on 4-inch silicon substrates covered by 300 nm thermal silicon oxide. Masks were defined using electron beam lithography (EBL, Vistec EBPG500+ operating at 100 kV) and metallic layers deposited using multi-angle shadow evaporation in an electron-beam evaporator. Directly on top of the substrate, ground planes and gate electrodes were formed by deposition of a 2 nm titanium adhesion layer, 30 nm gold, and a further 2 nm Ti protection layer over a mask defined in a single layer positive resist (Allresist AR-P6200). This initial deposition is covered, after lift-off, by a 50 nm insulating  $\text{Al}_2\text{O}_3$  layer grown by atomic layer deposition (ALD). On top of this layer, a second EBL metal evaporation process (2 nm Ti followed by 30 nm AuPd) is carried out to shape bonding pads and coarse electrodes connecting to the transistor leads and two tunnel probes, the rest of the bonding pads and electrodes are patterned in the third and final step. After a second lift-off process, NIS transistor and probe junctions, clean NS contacts and remaining bonding pads and electrodes are formed by EBL patterning on a Ge-based hard mask process [4]. The mask is composed of a  $\sim 400$  nm P(MMA-MMA) copolymer layer, covered by 22 nm Ge also deposited by e-gun evaporation and a thin (approximately 50 nm) layer of PMMA on top. After cleaving the wafer into smaller chips (typically  $1\text{ cm} \times 1\text{ cm}$ ), the pattern defined on the PMMA resist is transferred to the Ge layer by reactive ion etching (RIE) with  $\text{CF}_4$ . Next, an undercut profile is created in the copolymer layer by oxygen plasma in the same RIE. Creation of tunnel junctions is done first by evaporating a 30 nm layer of Al at a substrate tilt angle of  $-61.1^\circ$ , resulting in a film that defines the finger-like superconducting probes. Right after deposition, this layer is oxidized *in-situ* in the evaporator (static oxidation with typically 1.8 mbar for 1.5 minutes). A subsequent deposition of 30 nm Cu at approximately  $39.1^\circ$  tilt forms the normal-metal bolometers. Next, a second 30 nm layer of Al is evaporated at a tilt angle of  $-32.5^\circ$  defining the transistor leads and the NS clean contacts. After a second oxidation (nominally 1.7 mbar

$\text{O}_2$  for one minute), a final 40 nm Cu film was deposited at normal incidence forming the N island of the SINIS transistor. After a final conventional lift-off step, a chip with an array of  $3 \times 3$  devices is cleaved to fit a custom-made chip carrier and electrically connected to it by Al wire bonds for measurements.

### Measurements

A custom-made plastic dilution refrigerator with base temperature of about 100 mK was used to carry out measurements. DC signals were applied through conventional cryogenic signal lines (resistive twisted pairs between room temperature and the 1 K flange, followed by at least 1 m Thermocoax cable as a microwave filter to the base temperature) connecting the bonded chip to a room temperature breakout box. Driving signals were transported to the gate by rf lines consisting of stainless steel coaxial cable down to 4.2 K, a 20 dB attenuator in the liquid helium bath, followed by a feedthrough into the inner vacuum can of the cryostat. Inside the cryostat, the rf signal is carried by a continuous superconducting NbTi coaxial cable from the 1 K stage down to the sample carrier. At room temperature, an additional 40 dB attenuation is applied to the signal. Signals were realized by programmable voltage sources and function generators. Voltage and current amplification was achieved by room temperature low-noise amplifier (FEMTO Messtechnik GmbH, model DLPVA-100-F-D) and transimpedance amplifier (FEMTO Messtechnik GmbH, model DDPCA-300), respectively. The bath temperature is controlled by applying voltage to a heating resistor attached to the sample holder. The curves of the pumped current were typically repeated at least 10 times and averaged accordingly, neglecting those repetitions during which a random offset charge jump had occurred. Current amplifier offset was subtracted by comparing the pumping curves with their counterparts measured under source-drain bias of opposite polarity. The voltage drop curves across both bolometers were also repeated 15 times and averaged the same way as the current. After calibrating the bolometers' response against a previously calibrated ruthenium oxide thermometer (Scientific Instruments, Inc., model RO-600) attached to the cryostat sample carrier holder, the electronic temperature of the normal-metal trap is obtained by a linear fit to the response (see Supplementary Figure S3). Voltage amplifier offset is adjusted by comparing the response of the bolometer at equilibrium with its calibration curve and subtracting the difference.

## System modelling

The theoretical curves were obtained by calculating the current and power arising from the solution of a Markovian classical master equation on the island excess charge  $n$

$$\frac{d}{dt}p(n, t) = \sum_{n \neq n'} \gamma_{n'n} p(n', t) - \gamma_{nn'} p(n, t). \quad (3)$$

Here  $p(n, t)$  is the probability of the island to have  $n$  excess charges at time  $t$  and  $\gamma_{nn'}$  is the total transition rate from the state  $n$  to  $n'$  which is directly related to the tunnelling rates through a NIS interface. The equation is solved in the steady state ( $dp(n, t)/dt = 0$ ) for the DC regime and with periodic conditions ( $p(n, 0) = p(n, \tau)$ , with  $\tau = 1/f$ ) for the turnstile operation. The current through the left junction (L) is related to the occupation probabilities through

$$I_L = e \sum_n p(n) (\Gamma_{n \rightarrow n+1}^L - \Gamma_{n \rightarrow n-1}^L) + 2e \sum_n p(n) (\Gamma_{n \rightarrow n+2}^L - \Gamma_{n \rightarrow n-2}^L), \quad (4)$$

where  $\Gamma_{n \rightarrow n \pm 1}^L$  denotes the single-electron elemental process rates and  $\Gamma_{n \rightarrow n \pm 2}^L$  second order Andreev process rates. The current can be averaged along one cycle as  $\langle I_L \rangle = 1/\tau \int_0^\tau dt I_L$ .

The power injected to the transistor leads by stationary elementary events  $\dot{Q}_{n \rightarrow n \pm 1}^{R/L,S}$  gives the average injected power during one driving cycle as

$$\langle P_{R/L} \rangle = \frac{1}{\tau} \int_0^\tau dt \sum_n p(n) (\dot{Q}_{n \rightarrow n+1}^{R/L,S} + \dot{Q}_{n \rightarrow n-1}^{R/L,S}). \quad (5)$$

In contrast to the current, the individual elementary tunnelling events contribute always additively to the power. For the DC case and for calculating the instantaneous power the integral is omitted. For obtaining accurate results comparable to experiments and because of the stiffness of the time periodic problem, an alternative numerical solution to Eq. (3) based on propagation of the probability was carried out (see Supplementary Section S4). For further understanding of the instantaneous behavior of the quantities, Eq. (3) was also solved at discrete cycle intervals using a variable order method.

## ACKNOWLEDGEMENTS

We acknowledge O. Maillet and E. T. Mannila for useful discussions. This research made use of Otaniemi Research Infrastructure for Micro and Nanotechnologies (OtaNano) and its Low Temperature Laboratory. This work is funded through Academy of Finland grant 312057, European Union's Horizon 2020 research and

innovation programme under the European Research Council (ERC) programme (grant agreement 742559) and Russian Science Foundation (grant No. 20-62-46026).

## AUTHOR CONTRIBUTIONS

M.M.-S. made part of the fabrication, carried out the measurements, performed simulations and analysed the data with important input of J. P. P. and D. S. G. J.T.P. fabricated most part of the devices and prepared the measurement instruments. D. S. G. estimated the heat losses along the system. The primal idea was conceived by M.M.-S. and J.P.P. The manuscript was prepared by M.M.-S. with important input from J.P.P, J.T.P and D.S.G.

## COMPETING INTERESTS

The authors declare no competing interests.

## DATA AVAILABILITY

Data supporting the manuscript and supplementary Figures as well as further findings are available from the corresponding author upon reasonable request.

## CODE AVAILABILITY

The codes for generating the manuscript and supplementary Figures are available from the corresponding author upon reasonable request.

---

\* marco.marinsuarez@aalto.fi

- [1] Geerligs, L. J. *et al.* Frequency-locked turnstile device for single electrons. *Phys. Rev. Lett.* **64**, 2691–2694 (1990).
- [2] Kouwenhoven, L. P., Johnson, A. T., van der Vaart, N. C., Harmans, C. J. P. M. & Foxon, C. T. Quantized current in a quantum-dot turnstile using oscillating tunnel barriers. *Phys. Rev. Lett.* **67**, 1626–1629 (1991).
- [3] Pekola, J. P. *et al.* Hybrid single-electron transistor as a source of quantized electric current. *Nat. Phys.* **4**, 120 (2007).
- [4] Pekola, J. P. *et al.* Single-electron current sources: Toward a refined definition of the ampere. *Rev. Mod. Phys.* **85**, 1421–1472 (2013).
- [5] Kaestner, B. & Kashcheyevs, V. Non-adiabatic quantized charge pumping with tunable-barrier quantum dots: a review of current progress. *Rep. Prog. Phys.* **78**, 103901 (2015).

- [6] Giblin, S. P. *et al.* Realisation of a quantum current standard at liquid helium temperature with sub-ppm reproducibility. *Metrologia* **57**, 025013 (2020).
- [7] BIPM. *Mise en pratique for the definition of the ampere and other electrical units in the SI*, chap. Appendix 2 (Bureau international des poids et mesures, 2019), ninth edn. URL <https://www.bipm.org/en/publications/mises-en-pratique>.
- [8] Zwinkels, J. C., Ikonen, E., Fox, N. P., Ulm, G. & Rastello, M. L. Photometry, radiometry and 'the candela': evolution in the classical and quantum world. *Metrologia* **47**, R15–R32 (2010).
- [9] Chunnillall, C. J., Degiovanni, I. P., Kück, S., Müller, I. & Sinclair, A. G. Metrology of single-photon sources and detectors: a review. *Opt. Eng.* **53**, 081910 (2014).
- [10] Vaigu, A. *et al.* Experimental demonstration of a predictable single photon source with variable photon flux. *Metrologia* **54**, 218–223 (2017).
- [11] Rodiek, B. *et al.* Experimental realization of an absolute single-photon source based on a single nitrogen vacancy center in a nanodiamond. *Optica* **4**, 71 (2017).
- [12] Lemieux, S., Giese, E., Fickler, R., Chekhova, M. V. & Boyd, R. W. A primary radiation standard based on quantum nonlinear optics. *Nat. Phys.* **15**, 529–532 (2019).
- [13] Saha, S., Jaiswal, V. K., Sharma, P. & Aswal, D. K. Evolution of SI base unit candela: Quantifying the light perception of human eye. *MAPAN* **35**, 563–573 (2020).
- [14] Zhu, D. *et al.* Resolving photon numbers using a superconducting nanowire with impedance-matching taper. *Nano Lett.* **20**, 3858–3863 (2020).
- [15] Tomm, N. *et al.* A bright and fast source of coherent single photons. *Nat. Nanotechnol.* **16**, 399–403 (2021).
- [16] Palafox, L., Ramm, G., Behr, R., Ihlenfeld, W. K. & Moser, H. Primary AC power standard based on programmable josephson junction arrays. *IEEE Transactions on Instrumentation and Measurement* **56**, 534–537 (2007).
- [17] Waltrip, B. *et al.* AC power standard using a programmable josephson voltage standard. *IEEE Transactions on Instrumentation and Measurement* **58**, 1041–1048 (2009).
- [18] Waltrip, B. C., Nelson, T. L., Berilla, M., Flowers-Jacobs, N. E. & Dresselhaus, P. D. Comparison of AC power referenced to either PJVS or JAWS. *IEEE Transactions on Instrumentation and Measurement* **70**, 1–6 (2021).
- [19] Peltonen, J. T. *et al.* Thermal conductance by the inverse proximity effect in a superconductor. *Phys. Rev. Lett.* **105**, 097004 (2010).
- [20] Knowles, H. S., Maisi, V. F. & Pekola, J. P. Probing quasiparticle excitations in a hybrid single electron transistor. *Appl. Phys. Lett.* **100**, 262601 (2012).
- [21] Ullom, J. N., Fisher, P. A. & Nahum, M. Measurements of quasiparticle thermalization in a normal metal. *Phys. Rev. B* **61**, 14839–14843 (2000).
- [22] Giazotto, F., Heikkilä, T. T., Luukanen, A., Savin, A. M. & Pekola, J. P. Opportunities for mesoscopics in thermometry and refrigeration: Physics and applications. *Rev. Mod. Phys.* **78**, 217–274 (2006).
- [23] Dorozhkin, S., Lell, F. & Schoepe, W. Energy relaxation of hot electrons and inelastic collision time in thin metal films at low temperatures. *Solid State Commun.* **60**, 245–248 (1986).
- [24] Dynes, R. C., Narayanamurti, V. & Garno, J. P. Direct measurement of quasiparticle-lifetime broadening in a strong-coupled superconductor. *Phys. Rev. Lett.* **41**, 1509–1512 (1978).
- [25] Ronzani, A. *et al.* Tunable photonic heat transport in a quantum heat valve. *Nat. Phys.* **14**, 991–995 (2018).
- [26] Rajauria, S. *et al.* Andreev current-induced dissipation in a hybrid superconducting tunnel junction. *Phys. Rev. Lett.* **100**, 207002 (2008).
- [27] Prance, J. R. *et al.* Electronic refrigeration of a two-dimensional electron gas. *Phys. Rev. Lett.* **102**, 146602 (2009).
- [28] Rey, M., Strass, M., Kohler, S., Hänggi, P. & Sols, F. Nonadiabatic electron heat pump. *Phys. Rev. B* **76**, 085337 (2007).
- [29] Arrachea, L., Moskalets, M. & Martin-Moreno, L. Heat production and energy balance in nanoscale engines driven by time-dependent fields. *Phys. Rev. B* **75**, 245420 (2007).
- [30] Kafanov, S. *et al.* Single-electronic radio-frequency refrigerator. *Phys. Rev. Lett.* **103**, 120801 (2009).
- [31] Hussein, R., Kohler, S. & Sols, F. Heat pump driven by the shot noise of a tunnel contact. *Physica E* **77**, 156–163 (2016).
- [32] Alegria, L. D. *et al.* High-energy quasiparticle injection into mesoscopic superconductors. *Nat. Nanotechnol.* **16**, 404–408 (2021).